



Morphology dependent photocatalytic efficacy of zinc ferrite probed for methyl orange degradation

HUAN-YAN XU*, BO LI and PING LI

School of Materials Science and Engineering, Harbin University of Science and Technology,
Harbin 150040, P. R. China

(Received 1 May, revised 11 July, accepted 12 July 2018)

Abstract: Zinc ferrite ($ZnFe_2O_4$) photocatalysts with different morphologies (sizes and shapes) were synthesized to explore the effect of morphology on their photocatalytic efficiency. The results obtained using field emission scanning electron microscopy (FESEM) revealed that the obtained samples had the needle-, cube-, granule- and plate-like morphology, labeled as NZFO, CZFO, GZFO and PZFO, respectively. X-ray diffraction (XRD) patterns showed that all the samples had the spinel structure of $ZnFe_2O_4$ without any other impurities. The calculated average crystallite size followed the order NZFO<GZFO<CZFO<PZFO. The surface area was inversely proportional to the average crystallite size and followed the order NZFO>GZFO>CZFO>PZFO. The photocatalytic efficiency for the degradation of methyl orange also followed the order NZFO>GZFO>CZFO>PZFO. The morphology-dependent photocatalytic efficiency of $ZnFe_2O_4$ was closely related with its crystallite size and surface area. The smaller the crystallite size was, the larger the surface area was, and the higher the photocatalytic efficiency was.

Keywords: $ZnFe_2O_4$; morphology; crystallite size; photocatalysis; adsorption.

INTRODUCTION

The rapid development of industrialization made various pollutants discharged into water environments, which has become a serious problem worldwide. Organic dyes have been widely used in the industries of textile, paper, cosmetic and leather. Since they might bring potential risks to the ecological environments and human health even at low concentration, more and more attention has been paid to the unconfined and untreated discharge of organic dyes into waters.¹ For this reason, the removal of organic dyes from effluents is emerging as an important and severe task that must be dealt with cautiously. Many methods have been developed to approach this objective, including adsorption, coagula-

* Corresponding author. E-mail: xuhuanyan@hrbust.edu.cn
<https://doi.org/10.2298/JSC180501060X>

ion, chemical precipitation, membrane filtration, biological degradation and advanced oxidation processes (AOPs).^{2–4} As a sort of AOPs, the photocatalytic technology has been regarded as a superior method for the mineralization of organic pollutants, attributed to its high efficiency, low cost and no secondary pollutants.³ Since Fujishima and Honda discovered the photolysis of H₂O at titanium dioxide (TiO₂) electrode in 1972,⁵ the research and application of photocatalytic technology made a boom all over the world. In a typical photocatalytic process, photons with energy contents higher than the band gap of semiconductor are absorbed and the electrons from its valence band (VB) are transferred to the conduction band (CB) leaving holes in the VB. The photogenerated electrons and holes can react with O₂ and H₂O (or OH[–]) to produce superoxide radicals (O₂^{•–}) and hydroxyl radicals (•OH), respectively, which can nonselectively degrade the organic molecules into H₂O, CO₂ and other inorganic oxides (depending on parent organic molecule).⁶ To date, many semiconductor materials, besides TiO₂, have been applied as effective photocatalysts for the degradation of organic pollutants under UV or visible light irradiation, such as g-C₃N₄,⁷ ZnO,⁸ BiVO₄,⁹ BiOCl,¹⁰ CdS¹¹ and so on. In addition, the spinel ferrites have been widely used as the photocatalysts because of their suitable band gaps and easy magnetic separation after completion of reactions.^{12,13}

Zinc ferrite (ZnFe₂O₄) has been regarded as an emerging semiconductor photocatalyst for the degradation of various organic compounds and dyes in the past decade, due to its appropriate band gap (~1.9 eV), photochemical stability and low cost.^{14,15} However, during the photocatalytic reactions, the photogenerated electron–hole pairs in ZnFe₂O₄ can be easily recombined, consequently reducing its photocatalytic efficiency.¹⁶ Improving the photocatalytic efficiency of a semiconductor usually implies the enhanced capability of light harvesting and the efficient separation of photogenerated electron–hole pairs.¹⁷ For these two purposes, many attempts have been made to decorate ZnFe₂O₄ photocatalyst such as making hybridized combination with TiO₂,¹⁸ ZnO,¹⁹ g-C₃N₄²⁰ and graphene.²¹ Otherwise, the morphology of a material including size and shape also has an important effect on its properties and applications.²² It has been reported that ZnFe₂O₄ with various morphologies could be synthesized by many methods such as mechanochemical method, co-precipitation method, polymer pyrolysis method, sol-gel auto-combustion method, template method, electrospinning method, hydrothermal method and spray drying method.^{23,24} Different morphologies can endow ZnFe₂O₄ with different particle dimensions and surface areas, which could have significant influence on its photocatalytic efficiency. The particle dimension can be a key factor that affects the recombination pathway of photogenerated electron–hole pairs and thereby determines its utilization efficiency on photons.²⁵ Furthermore, the surface area of a photocatalyst is closely related with its adsorption ability, that plays a critical role in the photocatalytic pro-

cess. Thus, it is of great importance to explore the effect of morphology on photocatalytic efficiency of ZnFe₂O₄. However, to date, the scientific reports on this research are scarcely published.

Herein we report the effect of morphology on the photocatalytic efficiency of ZnFe₂O₄. The ZnFe₂O₄ photocatalyst with needle-, cube-, granule- and plate-like morphology was synthesized by hydrothermal method, egg-white complexing sol-gel method, oxalate co-precipitation method and self-propagating sol-gel method, respectively. Degradation of an azo dye, methyl orange (MO, 10 mg L⁻¹), was employed to evaluate the photocatalytic efficiency of ZnFe₂O₄ with different morphologies.

EXPERIMENTAL

Synthesis of ZnFe₂O₄ with different morphologies

All the chemical reagents used in this study were of analytical grade without further purification. In the hydrothermal procedure, 1.72 g of ZnCl₂·2H₂O and 5.41 g of FeCl₃·6H₂O were dissolved into 50 mL deionized water under magnetic stirring. Then, the pH value of mixed solution was adjusted to 12 by NaOH. The resulting suspension solution was transferred to a 100 mL teflon-lined stainless steel autoclave and kept at 100 °C for 24 h. After filtering and washing with deionized water and absolute ethyl alcohol, ZnFe₂O₄ powder was obtained and labelled as NZFO. In the egg-white complexing sol-gel procedure, the egg-white was employed as the complexation agent. 15 mL deionized water and 30 mL fresh egg-white were completely mixed under magnetic stirring for 30 min and then slowly added into the mixed solution of Zn(NO₃)₂·6H₂O (2.97 g) and Fe(NO₃)₃·9H₂O (8.08 g). The yellow-brown emulsion was obtained after magnetic stirring of the gel product for 2 h and evaporated in a water-bath pot at 90 °C. Finally, the resulting red-brown powder was sintered at 800 °C for 3 h and the obtained ZnFe₂O₄ was marked as CZFO. In the oxalate co-precipitation procedure, 2.97 g of Zn(NO₃)₂·6H₂O, 8.08 g of Fe(NO₃)₃·9H₂O and 6.3 g H₂C₂O₄·2H₂O were fully mixed and ground in an agate mortar until the yellow paste product was obtained. After filtering and washing with absolute ethyl alcohol, the yellow precipitate was sintered at 900 °C for 2 h to gain ZnFe₂O₄, tagged as GZFO. In the self-propagating sol-gel procedure, immediately after dissolution of 2.97 g of Zn(NO₃)₂·6H₂O and 8.08 g of Fe(NO₃)₃·9H₂O in deionized water, citric acid was added under magnetic stirring in a stoichiometric ratio of 1.2-1.4. Then, the mixed solution was heated to 50 °C, adjusted to pH 7 by NH₃·H₂O. The resulting colloid product was dried at 90 °C in an oven until the shaggy dry gel was obtained. After grinding and washing, the dry gel was sintered at 800 °C for 3 h to obtain ZnFe₂O₄, marked as PZFO.

Characterization methods

The crystalline phase of ZnFe₂O₄ was detected by X-ray diffraction (XRD) using a PANalytical X'Pert X-ray diffractometer with CuK_α radiation ($\lambda = 0.15418$ nm) over 2θ range of 20–70°. The morphology of ZnFe₂O₄ was observed by field emission scanning electron microscopy (FESEM), operating on FEI Sirion 200 scanning electron microscope at the working voltage of 20 kV. The elemental composition of ZnFe₂O₄ was analyzed by energy dispersive X-ray spectroscopy (EDS). Their surface areas were determined by a Sibata SA-1100 surface area analyzer, based on nitrogen adsorption-desorption data at liquid nitrogen temperature. UV-Vis diffuse reflection spectra (UV-Vis DRS) were recorded to analyze the optical property of the obtained samples using an USB4000 UV-Vis spectrometer (Ocean

Optics) with an integral sphere. The reference sample (a standard template) was provided by South Africa Optics. According to the XRD results, Scherrer's equation ($D = K\lambda/\beta\cos\theta$), with the constant of 0.9, was used to calculate the average crystallite size of ZnFe_2O_4 from the full width at half maximum of (311) diffraction peak in XRD pattern.

Photocatalytic evaluation

The photocatalytic performance of ZnFe_2O_4 was evaluated using 10 mg L⁻¹ MO as the target pollutant under UV-light irradiation. All the adsorption and photocatalytic experiments were performed at room temperature. A 15W ZSZ15-40 UV lamp with UV-light wavelength of 365 nm was located at 15 cm above the beaker reactor. 0.1 g of ZnFe_2O_4 photocatalyst was weighed and placed into 100 mL MO solution with the concentration of 10 mg L⁻¹. Before irradiation by UV light, the suspension was stirred in the dark for 30 min to reach the adsorption–desorption equilibrium. Then, the UV light was turned on and photocatalytic reaction started under continuous stirring. At regular time interval of the reaction, a certain volume of the suspension solution was taken out and filtered by a quantitative filter paper to obtain the supernatant. The UV–Vis absorption spectra of the supernatant were recorded by an USB4000 UV–Vis spectrometer (Ocean Optics) in cells with 1 cm optical path length at room temperature.

RESULTS AND DISCUSSION

Characterization of ZnFe_2O_4 with different morphologies

The morphologies of ZnFe_2O_4 synthesized from different methods are illustrated in Fig. 1, where it can be seen that NZFO, CZFO, GZFO and PZFO display the needle-, cube-, granule- and plate-like shape, respectively. The particle dimension of these samples is different as well. The needle-like NZFO is about 400–500 nm in length and 30–40 nm in diameter; cube-like CZFO has inhomogeneous particle dimensions ranging from 100 to 700 nm in the length of the edge; granule-like GZFO has the diameters of approximately 200–300 nm; plate-

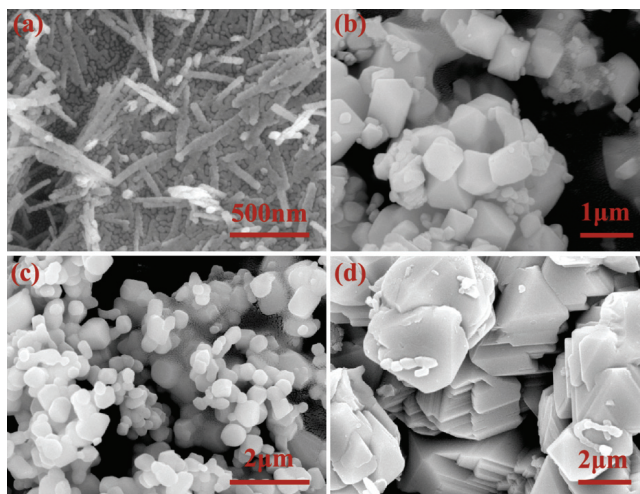


Fig. 1. FESEM images of: a) NZFO, b) CZFO, c) GZFO and d) PZFO.

-like PZFO presents the plate-stacking structures with the dimensions larger than 2 μm . The particle sizes obtained using FESEM are listed in Table I. The EDS pattern (Fig. 2) indicates that the elemental compositions of GZFO are Zn, Fe and O, without any other elemental impurities. The quantitative analysis revealed that the mole ratio of Zn, Fe and O was 1:1.5:4.18, which is close to the stoichiometric value of ZnFe₂O₄ and consistent with the previous study.²⁶ Likewise, there are no elemental impurities in NZFO sample, as shown in its EDS pattern (Fig. S-1 of the Supplementary material to this paper).

TABLE I. Particle sizes obtained using FESEM, average crystallite sizes calculated from XRD and specific surface area of NZFO, CZFO, GZFO and PZFO

Sample	Particle size measured using FESEM, nm	Average crystallite sizes calculated from XRD, nm	Specific surface area, $\text{m}^2 \text{g}^{-1}$
NZFO	400–500 in length, 30–40 in diameter	41	26.27
CZFO	100–700	125	5.38
GZFO	200–300	96	9.04
PZFO	>2000	163	3.92

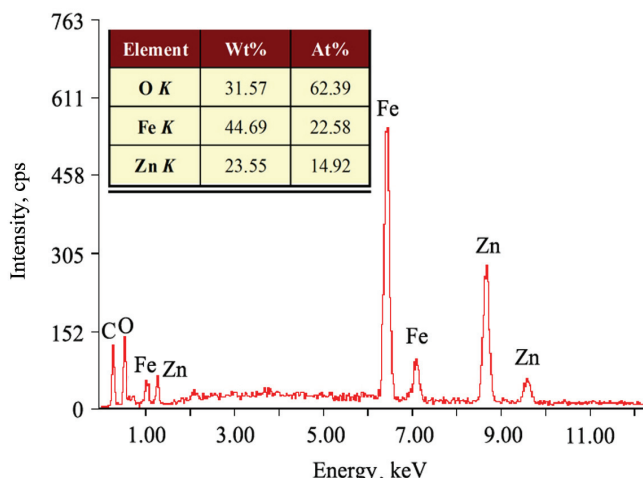


Fig. 2. EDS pattern of GZFO sample.

Fig. 3 displays the XRD patterns of ZnFe₂O₄ with different morphologies. It can be seen that all the samples have spinel structure with the characteristic diffraction peaks at 2θ 29.8, 35.3, 36.9, 43.0, 53.1, 56.6 and 62.1°, corresponding to (220), (311), (222), (400), (422), (511) and (440) crystal planes, respectively (JCPDS 22-1012).²⁶ No diffraction peaks of other phases can be found, indicating the presence of a single phase of ZnFe₂O₄ for all the samples. Based on the Scherrer's Equation, the average crystallite size of these samples was calculated and the results are listed in Table I. These data clearly indicate that the average

crystallite size of these samples follows the order NZFO<GZFO<CZFO<PZFO. The calculated values are in the range of 41–163 nm, which is much greater than those reported in other publications.^{26,27}

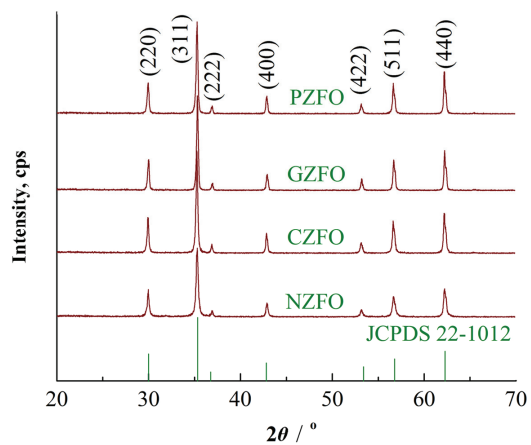


Fig. 3. XRD patterns of NZFO, CZFO, GZFO and PZFO.

The possible reason suggested for this phenomenon might be that no surfactants were added in the four synthesis routes in this study. It has been generally accepted that the formation of nanoparticles goes through two stages, *i.e.*, the generation of a large crystal nucleus and the growth of the nucleus. When a surfactant was introduced into the synthesis route, it might be adsorbed on the crystal nucleus surface, consequently restraining the nucleus growth and stabilizing the nanoparticles.²⁸ In this study, no surfactants were used, so the average crystallite size was greater than that of the samples synthesized in the presence of a surfactant. Furthermore, the observed size of ZnFe₂O₄ particles in FESEM images was much larger than that calculated from XRD results. This might be attributed to the fact that the calculated size was the average value of a single crystallite and the observed particle was the agglomerate of many ZnFe₂O₄ crystallites, and amorphous parts as well.²⁹ As expected, the surface areas of these samples were inversely proportional to their average particle sizes and, as listed in Table I, they follow the order NZFO>GZFO>CZFO>PZFO. UV–Vis DRS spectra (Fig. S-2 of the Supplementary material) indicate that NZFO, CZFO, GZFO and PZFO have similar optical absorption thresholds, suggesting no obvious difference in their optical structures. Based on UV–Vis DRS, the band gap (E_g) of these obtained samples can be determined by the extrapolation of the linear portion of $(F(R) \cdot h\nu)^{0.5}$ curve versus photon energy $h\nu$ to $[F(R) \cdot h\nu]^{0.5} = 0$.³⁰ As shown in Fig. S-3 of the Supplementary material, the E_g values of NZFO, CZFO, GZFO and PZFO are 1.81, 1.84, 1.83 and 1.84 eV, respectively. This also indicates they have similar band gaps.

Photocatalytic performance of $ZnFe_2O_4$ with different morphologies

Under UV light irradiation, as can be seen in Fig. 4 and S-4, MO can be effectively decomposed with all applied samples. UV–Vis absorption spectra of MO during photodegradation over NZFO are presented in Fig. 4 and it shows that the UV–Vis absorption peak of MO solution around 480 nm gradually weakens and disappears after 180 min reaction time, suggesting that almost all the MO molecules were mineralized into carbon dioxide, water and small-molecular-weight substances.

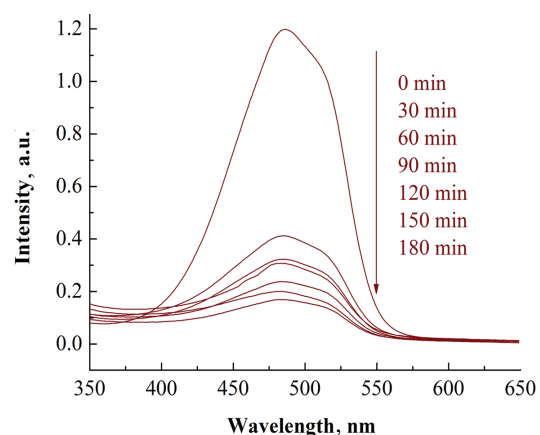


Fig. 4. UV–Vis absorption spectra of MO solution after different reaction periods over NZFO.

The kinetic curves presented in Fig. 5a clearly indicates that the photocatalytic efficiency of $ZnFe_2O_4$ for MO degradation follows the order NZFO>GZFO>CZFO>PZFO. In regard to NZFO, nearly 87 % MO could be removed after 180 min reaction, exhibiting the highest photocatalytic activity. However, only 53 % MO could be removed when PZFO was used as the photocatalyst. It has been demonstrated that the photocatalytic efficiency of $ZnFe_2O_4$ photocatalysts rises with the increase in their specific surface area, resulting from its decreased particle size.¹⁵ Furthermore, it should be noted that, at the adsorption-desorption equilibrium, the saturated adsorption capacity of MO onto different samples also follows the order NZFO>GZFO>CZFO>PZFO. This strongly implied that the morphology-dependent photocatalytic efficiency of $ZnFe_2O_4$ was closely related to its specific surface area. $ZnFe_2O_4$ with different morphologies had different particle sizes and specific surface areas. The smaller the particle size was, the larger the specific surface area was, and the higher the photocatalytic efficiency was. The specific surface area played an important role in the photocatalytic process for the degradation of organic dyes. Higher specific surface area could result in higher adsorption of a dye molecule onto the surface of photocatalyst and consequently improve the photocatalytic efficiency.³¹

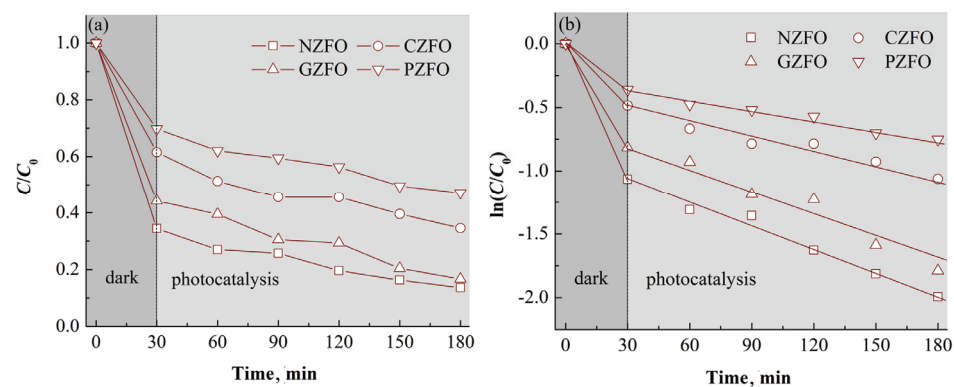


Fig. 5. a) Kinetic curves and b) pseudo-first-order kinetic analysis on the photocatalytic degradation of MO over ZnFe₂O₄ with different morphologies.

Fig. 5b indicates that the photocatalytic degradation of MO over different samples follows the pseudo-first-order kinetic model: $\ln(C/C_0) = kt$, where C_0 is the initial MO concentration, C is the residual MO concentration at time t , and the slope k is the reaction rate constant. Their apparent reaction rate constants were obtained from the slope of fitted line and are shown in Fig. 6, where it can be seen that the reaction rate constants of MO degradation over NZFO and GZFO are larger than those over CZFO and PZFO. This might also be attributed to their larger specific surface areas, which would make more MO molecules adsorbed onto photocatalyst surface and enhance its photocatalytic efficiency. Moreover, the stability of a photocatalyst is another important parameter that can influence its photocatalytic activity. The recyclability of ZnFe₂O₄ with different morphologies was evaluated as well. Fig. 7 indicates that, even after 4 cycles, ZnFe₂O₄ samples with different morphologies still maintain almost unchanged

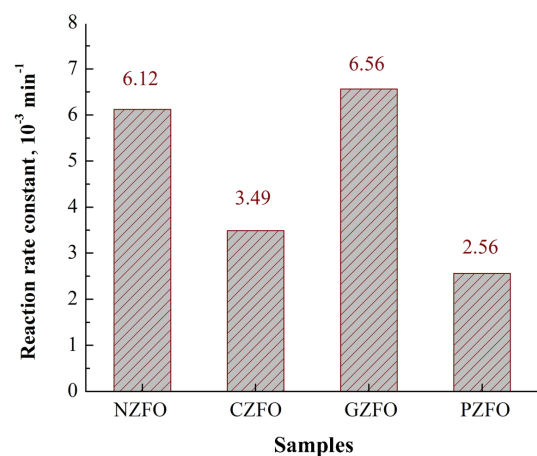


Fig. 6. Reaction rate constants of MO photocatalytic degradation over different ZnFe₂O₄ samples.

adsorption capacity and photocatalytic activity, showing high photocatalytic stability.

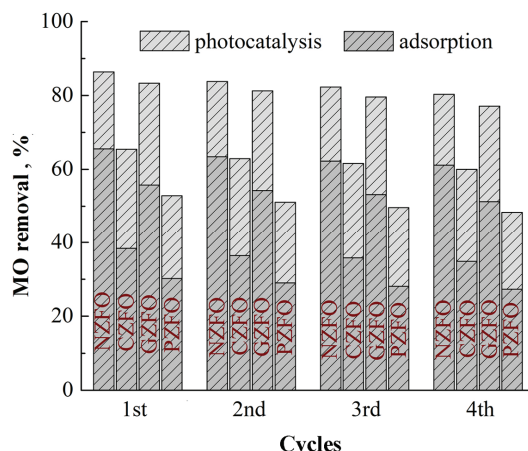


Fig. 7. Cycle tests for different samples to remove MO.

CONCLUSION

ZnFe₂O₄ with needle-, cube-, granule- and plate-like morphology were synthesized in this work. The average particle sizes of these samples followed the order NZFO<GZFO<CZFO<PZFO. Their specific surface areas were inversely proportional to the average particle sizes and followed the order NZFO>GZFO>CZFO>PZFO. The photocatalytic efficiency of ZnFe₂O₄ for MO degradation also followed the order NZFO>GZFO>CZFO>PZFO, as well as their saturated adsorption capacity of MO. Hence, the morphology-dependent photocatalytic efficiency of ZnFe₂O₄ was closely related with its particle sizes and specific surface areas.

SUPPLEMENTARY MATERIAL

Additional experimental data are available electronically at the pages of the journal website: <http://www.shd.org.rs/JSCS/>, or from the corresponding author on request.

И З В О Д
ФОТОКАТАЛИТИЧКА ЕФИКАСНОСТ ЦИНК-ФЕРИТА РАЗЛИЧИТЕ МОРФОЛОГИЈЕ
У ПРОЦЕСУ РАЗГРАДЊЕ МЕТИЛ-ОРАНЖА

HUAN-YAN XU, BO LI и PING LI

*School of Materials Science and Engineering, Harbin University of Science and Technology, Harbin 150040,
P. R. China*

Синтетисани су цинк-феритни (ZnFe₂O₄) фотокатализатори различите морфологије да би се испитао утицај морфологије на њихову фотокаталитичку ефикасност. Резултати добијени скенирајућом електронском микроскопијом су показали да синтетисани узорци NZFO, CZFO, GZFO и PZFO садрже игличасте, коцкасте, сферичне и плочасте честице, редом. Рендгенска дифракционана анализа је показала да сви узорци садрже чист ZnFe₂O₄ спинелне структуре, без примеса. Величина кристалита синтетисаних узорака

се повећава у низу NZFO<GZFO<CZFO<PZFO. Специфична површина је обрнуто пропорционална величини кристалита и опада у низу NZFO>GZFO>CZFO>PZFO, као и фотокатализитичка ефикасност у процесу разградње метил-оранџа. Закључено је да фотокатализитичка ефикасност цинк-ферита различите морфологије зависи од величине кристалита и специфичне површине: што су кристалити мањи, специфична површина је већа, а тиме и фотокатализитичка ефикасност.

(Примљено 1. маја, ревидирано 11. јула, прихваћено 12. јула 2018)

REFERENCES

- K. He, G. Q. Chen, G. M. Zeng, A. W. Chen, Z. Z. Huang, J. B. Shi, T. T. Huang, M. Peng, L. Hu, *Appl. Catal., B: Environ.* **228** (2018) 19
- A. Hassani, P. Eghbali, A. Ekicibil, O. Metin, *J. Magn. Magn. Mater.* **456** (2018) 400
- Z. M. Fard, M. Bagheri, H. Z. Mousavi, S. Rabieh, *Mater. Res. Bull.* **101** (2018) 311
- F. Li, J. H. Huang, Q. Xia, M. M. Lou, B. Yang, Q. Tian, Y. B. Liu, *Sep. Purif. Technol.* **195** (2018) 83
- A. Fujishima, K. Honda, *Nature* **238** (1972) 37
- S. M. Alipour, D. Friedmann, J. Scott, R. Amal, *J. Hazard. Mater.* **341** (2018) 404
- L. Svoboda, P. Praus, M. J. Lima, M. J. Sampaio, D. Matysek, M. Ritz, R. Dvorsky, J. Faria, C. Silva, *Mater. Res. Bull.* **100** (2018) 322
- A. Das, P. Malakar, R. G. Nair, *Mater. Lett.* **219** (2018) 76
- Y. Hu, W. Chen, J. P. Fu, M. W. Ba, F. Q. Sun, P. Zhang, J. Y. Zou, *Appl. Surf. Sci.* **436** (2018) 319
- C. Y. Wang, Y. J. Zhang, W. K. Wang, D. N. Pei, G. X. Huang, J. J. Chen, X. Zhang, H. Q. Yu, *Appl. Catal., B: Environ.* **221** (2018) 320
- R. Lei, H. W. Ni, R. S. Chen, H. Z. Gu, B. W. Zhang, W. T. Zhan, *J. Colloid Interf. Sci.* **514** (2018) 496
- E. Casbeer, V. K. Sharma, X. Z. Li, *Sep. Purif. Technol.* **87** (2012) 1
- M. Sundararajan, V. Sailaja, L. J. Kennedy, J. J. Vijaya, *Ceram. Int.* **43** (2017) 540
- R. X. Shi, Y. Zhang, X. T. Wang, Q. Ma, A. Y. Zhang, P. Yang, *Mater. Chem. Phys.* **207** (2018) 114
- S. D. Jadhav, P. P. Hankare, R. P. Patil, R. Sasikala, *Mater. Lett.* **65** (2011) 371
- G. Q. Hou, Y. J. Zhang, S. J. Gao, *Mater. Lett.* **209** (2017) 598
- Y. Li, Y. Z. Li, Y. D. Yin, D. H. Xia, H. R. Ding, C. Ding, J. Wu, Y. H. Yan, Y. Liu, N. Chen, P. K. Wong, A. H. Lu, *Appl. Catal., B: Environ.* **226** (2018) 324
- H. G. Fan, D. D. Chen, X. F. Ai, S. Han, M. B. Wei, L. L. Yang, H. L. Liu, J. H. Yang, *RSC Adv.* **8** (2018) 1398
- Y. Xu, S. M. Wu, X. L. Li, Y. H. Huang, Z. P. Wang, Y. D. Han, J. B. Wu, H. Meng, X. Zhang, *New J. Chem.* **41** (2017) 15433
- S. W. Zhang, J. X. Li, M. Y. Zeng, G. X. Zhao, J. Z. Xu, W. P. Hu, X. K. Wang, *ACS Appl. Mater. Interf.* **5** (2013) 12735
- Y. S. Fu, X. Wang, *Ind. Eng. Chem. Res.* **12** (2011) 7210
- B. S. Mwankemwa, S. Akinkuade, K. Maabong, J. M. Nel, M. Diale, *Physica B* **535** (2018) 175
- J. T. Yan, S. Y. Gao, C. L. Wang, B. Chai, J. F. Li, G. S. Song, S. Z. Chen, *Mater. Lett.* **184** (2016) 43
- M. Qin, Q. Shuai, G. L. Wu, B. H. Zheng, Z. D. Wang, H. J. Wu, *Mater. Sci. Eng., B* **224** (2017) 125
- F. Amano, E. Ishinaga, A. Yamakata, *J. Phys. Chem., C* **117** (2013) 22584

26. E. Aghabeikzadeh-Naeini, M. Movahedi, N. Rasouli, Z. Sadeghi, *Mater. Sci. Semicond. Process.* **73** (2018) 72
27. M. Dhiman, R. Sharma, V. Kumar, S. Singhal, *Ceram. Int.* **42** (2016) 12594
28. V. Vaiano, O. Sacco, D. Sannino, P. Ciambelli, *Appl. Catal., B: Environ.* **170** (2015) 153
29. H. Y. Xu, Z. Zheng, G. J. Mao, *J. Hazard. Mater.* **175** (2010) 658
30. H. Y. Xu, L. C. Wu, L. G. Jin, K. J. Wu, *J. Mater. Sci. Technol.* **33** (2017) 30
31. S. Natarajan, H. C. Bajaj, R. J. Tayade, *J. Environ. Sci.* **65** (2018) 201.